Characterisation of Local Damage in Pultruded GFRP Road Bridge Decks with Random Fibre Mat Misalignments

M. Poulton[1], W.M. Sebastian[1,*]

[1]Department of Civil, Environmental and Geomatic Engineering, University College London, Chadwick Building, Gower Street, London, WC1E 6BT, UK

Corresponding author email address: w.sebastian@ucl.ac.uk

Abstract:

The extent to which random, manufacturing-induced fibre mat misalignments compromise the structural integrity of pultruded GFRP road bridge decks is not fully understood. The problem is often critical at the web-flange junctions, which frequently contain the most severe misalignments and are subjected to high moment-shear (M-V) combinations due to local tyre load effects. To that end, in the presently reported experimental study, determinate M-V combinations were applied at the junctions of a pultruded GFRP bridge deck, without artificially restraining (e.g. by clamping, which spuriously strengthens) these junctions. For any given M-V ratio, significant scatter was observed in the damage patterns and loads up to ultimate, owing to random fibre mat misalignments which have been digitally documented in a previous paper. Damage occurred mostly within the junctions, and sometimes in the adjoining flanges. Relative to misalignment-free specimens, the first fracture moments dropped by 19% and 21% for junctions containing flip and wrinkle misalignments respectively. 19% of tests showed higher tangent stiffnesses after damage, probably due to beneficial changes in load-carrying mechanism. A three-pronged approach, based on the load-response, acoustic emission and video data, enables the definition of damage indices, thereby paving the way for integrity assessment of pultruded decks under local tyre load effects.

Keywords: Glass fibres, fabrics/textiles, defects, pultrusion

1. Introduction

Pultrusion is one of the most popular manufacturing techniques for glass fibre reinforced polymer (GFRP) structures used in civil engineering, including bridge decks [1]. Pultrusion enables the continuous production of modular, cellular profiles with various fibre architectures that are difficult to produce using other manufacturing techniques [2]. The high strength-to-weight ratios of both the GFRP material and the cellular design can result in decking systems that are 80% lighter than equivalent reinforced concrete alternatives, and with superior long-term performance [3].

The structural performance of GFRP decks is strongly influenced by the local response of their web-flange junctions to tyre patch loading on the nearby top flange [4]. Under the patch loads, these junctions transmit high, multi-directional stress resultants whether the deck runs transversely as in the UK's West Mill bridge [5] or longitudinally as in the UK's Frampton Cotterell bridge [6]. Such large stress resultants transmitted through the small volumes of the junctions lead to high local stresses that are further magnified by the randomly misaligned fibre mat layers present in the junction due to imperfect quality control during the manufacturing process [7]. Misalignments refer to out-of-plane deviations of the fibre mats (for example, waviness, wrinkles and folds) from their optimal trajectories; that is, the trajectories that produce the greatest load-carrying capacity in service.

Note that the misalignments do not reduce the stress *capacity* of the material, rather they increase the local (normal and shear) stress *demands* along and near the misaligned fibre layer, which reduces the structural integrity of the junctions. Indeed, previous tests have shown that the misaligned fibres dominate the failure behaviours of the junctions in pultruded decks [8–15] and in I-sections [16–21], which in turn has led to serviceability problems for FRP decks on the road networks in different countries [22,23]. For FRP components used in the aerospace, automotive, renewable energy and marine domains, such as stiffened panels employed in aircraft, F1 cars, wind turbines and yachts, these misalignments and their associated knock-down effects have been extensively studied [24–28].

However, for the civil engineering application of FRP bridge decks manufactured by pultrusion and other methods, this issue has received relatively limited attention. In one of the very few relevant studies [29] to date on this topic, loads up to junction failure were applied to the deck in a test setup that preserves the load paths within the deck and minimizes artificial boundary conditions (e.g. clamping, which can spuriously strengthen the joint), whilst maintaining statical determinacy of the stress resultants on the junctions. This was achieved by making a cut across the width of the top flange, to create a top flange cantilever (e.g. see Figure 2(a)) rooted at the GFRP deck's internal junction. The different individual and bonded junction configurations for a given decking system were studied. The focus was on illustrating the test method, so each test was performed once, which meant that the extent of scatter in the junctions' structural characteristics was not evaluated. This study also presented a manual method for mapping the misalignments. A subsequent study [7] built on this initial investigation by presenting a *digitized* method of mapping the misalignments. This study also presented a dual scheme for defining a *taxonomy* of these misalignments, including the geometry and the origins in specific features of the manufacturing process.

It is now appropriate to further expand on these earlier studies by understanding the influence of the scatter in misalignment geometry on any associated variation in the failure behaviour of the junctions. To that end, an important manufacturing distinction between pultruded and non-pultruded junctions should now be highlighted. Non-pultruded junctions, which are typically resin-infused or prepreg-based, are manufactured in a multi-stage process by either co-bonding or adhesively bonding L-shaped sections (stiffeners) to a flat sheet (skin). This process leaves a triangular-shaped region (or deltoid) at the centre of the junction, commonly filled with uni-directional fibres or resin, and the failure *mode* of these junctions is often dominated by delamination of the deltoid from the stiffeners and/or skin [30]. Within this failure mode, the damage loads can be quite variable owing to manufacturing-induced variability of the deltoid shape, which for co-bonded junctions can produce misalignment of the surrounding plies. One study [31] showed that, as a result, a 46% reduction in deltoid area produced a 33% reduction in tensile capacity. By contrast, pultruded deck junctions exhibit multiple failure modes, each with significant scatter in the failure loads, owing to the range of types and spatial locations of the misalignments. Therefore, the failure mechanics of non-pultruded junctions are of limited value in assessing pultruded junctions. Instead, investigations specific to pultruded junctions must be conducted.

Previous studies have considered flat FRP coupons under axial load [32–35], and so the knock-down effects of the misalignments were expressed as reductions of tensile or compressive capacity of the section. Bridge deck junctions, however, are subjected to combinations of local bending moment and vertical shear, for which a moment-shear interaction failure envelope seems a more natural means of quantifying knock-down effects.

Acoustic Emission (AE) sensors can aid the detection and quantification of damage within the deck's junctions. AE is defined as a transient elastic wave generated by material fracture leading to structural damage [36]. Changes in the cumulative AE hits or energy plots are commonly used in conjunction with mechanical data to identify the initiation of damage. Previous studies have applied AE damage identification to flat FRP coupons [37], and to adhesively bonded joints of pultruded components [38,39], which gave confidence in the application to the T-shaped junctions of the present study. This study also builds on previous work by introducing novel damage indices which fuse the AE data with the load-displacement data and also with visual observations from high-resolution video records of the junctions.

The objectives of the present study, for the web-flange junctions of a specific deck system, are to:

- Perform repeat tests to ultimate that enable definition of the moment-shear failure envelopes of the junctions including the effects of scatter.

- Combine the load-displacement data, AE data and video logs to characterise the initiation and progression of damage, by defining damage indices, in the junctions up to failure.
- Relate the scatter in failure loads and the severity of damage to the degree of fibre mat misalignment.

In what follows, the test methodology is described, the key results are reported, then a detailed analysis relating the misalignment profile to the severity of damage is presented, and finally conclusions are drawn.

2. Methodology

2.1 Description of GFRP deck specimens

Figure 1 shows the geometry of the GFRP deck used in this study, which is a rectangular unit that encloses two inclined webs to form three cells. The GFRP material consists of E-glass fibre mats and rovings embedded in an isophthalic polyester resin. This deck has been used in highway and pedestrian bridges around Europe, including a 73m span pedestrian bridge in Germany completed in 2019 [40]. The top flange of the deck is thicker (9 mm) than the bottom flange (6 mm) to provide adequate resistance to local tyre loads.

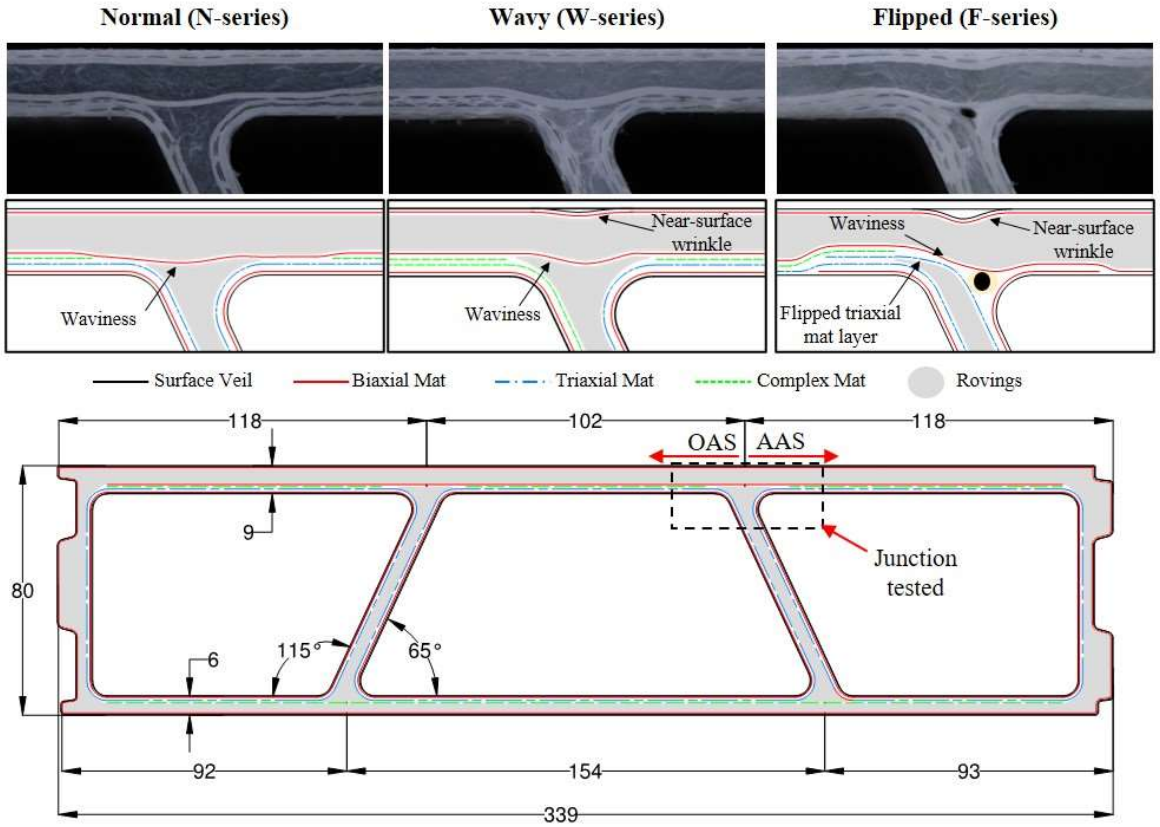

Figure 1: Geometry of GFRP deck with illustrations of the fibre mat positions

From resin burn-off tests, the fibre architecture was observed to comprise rovings, a surface veil, and three types of mat: a triaxial mat with +45°, -45° and 0° fibre bundles, a biaxial mat with 90° and 0° bundles and a complex mat that consisted of 90°/0° woven bundles stitched to a layer of continuous filament mat (CFM). The unidirectional rovings formed a single, thick layer within the core of the material, and on the outer surfaces there was a veil that consisted primarily of CFM and 0° bundles. The diagram at the bottom of Figure 1 shows how these mats and rovings were arranged in the deck.

Tests were conducted only on the internal junction at the top of the right-hand inclined web, which is labelled in Figure 1. Henceforth, the left- and right- hand sides of the junction as seen in Figure 1 are referred to as OAS (obtuse angle side) and AAS (acute angle side), respectively. Junctions from *three* different pultrusion batches were selected for testing, named Normal (N-series), Wavy (W-series) and Flipped (F-series), images of which are shown at the top of Figure 1.

At this point, it is useful to briefly summarise the taxonomy of fibre mat misalignments defined in a previous study [7], which is of direct relevance to the study presented in this paper. In that earlier study, six different categories of misalignment were identified within the junctions of different batches of the very pultruded GFRP deck system used in the present study. The categories were defined from the observed shapes and manufacturing provenances of the misalignments. The six categories (some of which are illustrated in Figure 1) were: double-back, flip, corner wrinkle, near-surface wrinkle, waviness and drop. For waviness, the misalignment severity was quantified using the angle to its steepest tangent, its length, and its height; while for near-surface wrinkles, the amplitude and width of a fitted Gaussian function were used. That earlier study reported significant variation in misalignment severity between junctions from different pultrusion batches.

In the present study, three different categories of misalignment were observed within the selected junctions, which are labelled in Figure 1: a flipped triaxial mat layer, a near-surface wrinkle at the top of the junction, and waviness of the biaxial mat in the middle of the junction. The flip was only present in the F-series, whereas the wrinkle and waviness were present to varying degrees in all three junction types. The scatter in degree of wrinkling and waviness is presented in Section 4.1. Finally, the fibre layups were identical for each junction, except for the W-series that, on the OAS side, had a complex mat in place of a triaxial mat layer.

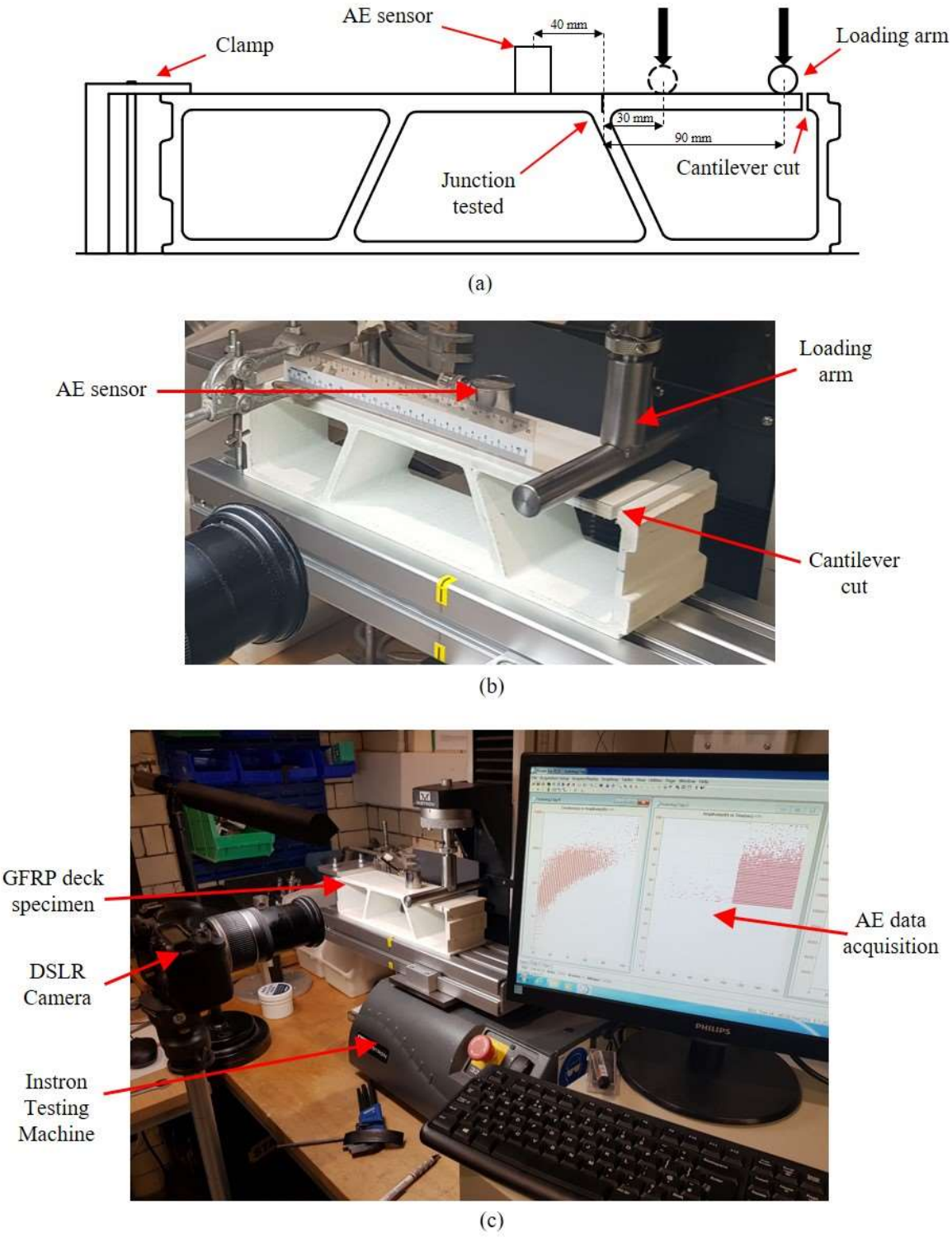

Figure 2: (a) Diagram of test setup, (b) close-up image of specimen and (c) image of instrumentation.

2.2 Experimental setup and loading strategy

Preparation of the GFRP deck specimens was undertaken in two steps: (i) the bridge deck panels were cut into 80 mm wide specimens; (ii) a top flange cantilever rooted at the internal junction was created by cutting

across the 80 mm width of this flange near to the external right-angle junction, as shown in Figure 2(a) and in the close-up image of the specimen in Figure 2(b). The 80 mm width was chosen to ensure the junctions failed within the 5 kN load capacity of the testing machine. It is important to note that the GFRP deck was initially provided in seven short panels, typically 330 mm wide, of which two contained a 'Normal' junction, two a 'Wavy' junction, and three a 'Flipped' junction. It was possible to cut four 80 mm wide specimens from most panels. The specimens cut from the same deck panel are assigned to a unique subgroup, and the mat misalignments and failure behaviours of these subgroups are presented independently throughout the remainder of the paper.

Figure 2(c) shows an image of the experimental setup that includes the test machine, real-time AE acquisition data displayed on the monitor, and video camera. The tests were conducted on an Instron 3345, which had a compressive load capacity of 5 kN. The load was applied using a 100 mm wide, 20 mm diameter steel bar placed across the width of the cantilever, with a 1 mm thick rubber strip between this bar and the specimen to prevent local crushing of the GFRP material. The distance from the centreline of the junction to that of the loading arm was varied between 30 mm and 90 mm, see Figure 2(a).

The specimens were secured to the machine using a clamp applied directly above the vertical web on the opposite side of the junction being tested (Figure 2(a)). This acted as a translational and rotational restraint that adequately replicated the in-situ boundary conditions, whereby the deck would be adhesively bonded to adjacent units. The cantilever was loaded under displacement control at a rate of 1.8 mm/min, which is within the range recommended by BS ISO 15024:2001 [41] for a double cantilever beam test on GFRP specimens. The vertical force and displacement were acquired at a rate of 100 Hz from the Instron machine using Bluehill 3 software.

The AE system comprised a single R15I-AST resonant-type sensor with an operating frequency range of 50-400 kHz and a resonant frequency of 150 Hz, provided by Physical Acoustic Corporation. The sensor had an integral preamplifier with an electrical gain of 40 dB. The AE signals were recorded by a PCI-2 based acquisition computer using the AEwin software at a sampling rate of 2 MHz. Silicone grease was used as the acoustic coupling agent. As shown in Figure 2(a) and (b), the sensor was placed on the top surface of the deck, 40 mm from the centreline of the junction. This offset was necessary due to the surface cracks that developed directly above the junction during failure that would have decoupled the sensor. A pencil-lead break procedure was used to ensure good conductivity between the sensor and GFRP material [42]. Incoming waves were converted to a voltage signal by the sensor and were recorded as a hit when the voltage amplitude exceeded the

threshold level set to 45 dB. This value adequately removed background noise whilst ensuring that even low-amplitude AE events emanating from the GFRP material were detected. The absolute energy of each recorded hit was derived from the integral of the squared voltage signal divided by the reference resistance (10k-ohm).

The cross-sectional surface of the junction during failure was recorded using a Canon 7D DSLR camera with a 200 mm telephoto zoom lens at a frame rate of 24 Hz.

2.3 Summary of tests conducted

Table 1 provides a summary of the 28 tests performed on the three primary junction types. The junction subgroups are assigned a letter based on the type (e.g. 'N' for Normal) and a number that distinguishes between different deck panels (1, 2, 3 … etc.). Typically, there were four specimens per subgroup, except for N-2 and F-3 that had three and five specimens, respectively. The test code (right column of Table 1) is simply the subgroup code with a third number indicating the lever arm distance applied during that test. Note that although the majority of tests were conducted at regular lever arm intervals of 30, 50, 70, and 90 mm, some tests were performed at 40, 60 and 80 mm. In total, there were 7 tests for the N-series, 8 for the W-series and 13 for the F-series.

Table 1: Summary of cantilever tests

Junction type	Junction subgroup	Lever arm distance (mm)	Test code
Normal (N)	N-1	40, 50, 60, 80	N-1-40, N-1-50, N-1-60, N-1-70
Normal (N)	N-2	30, 60, 90	N-2-30, N-2-60, N-2-90
Wavy (W)	W-1	30, 50, 70, 90	W-1-30, W-1-50, W-1-70, W-1-90
Wavy (W)	W-2	30, 50, 70, 90	W-2-30, W-2-50, W-2-70, W-2-90
Flipped (F)	F-1	30, 50, 70, 90	F-1-30, F-1-50, F-1-70, F-1-90
Flipped (F)	F-2	30, 50, 70, 90	F-2-30, F-2-50, F-2-70, F-2-90
Flipped (F)	F-3	40, 50, 60, 70, 80	F-3-40, F-3-50, F-3-60, F-3-70 F-3-80

3. Key results

Failure of the junctions consisted of a series of distinct crack initiation events, each of which corresponded to one of *four* damage modes. Figure 3 shows, for each junction type, example images of the four damage modes, which are described below:

- Mode D_c: delamination within the corner of the junction's OAS side, combined with a transverse crack within the web's roving core that extended from the base of the delamination across the

width of the web. For the N- and F- series, the delamination occurred between the +45° and -45° fibre layers within the triaxial mat, whereas in the W-series the delamination occurred between the complex mat and roving layers.

- Mode D_t: delamination at the top of the junction between the wrinkled 90° fibre layer and the roving layer, combined with a transverse crack within the roving layer that extended diagonally from the right edge of the delamination to the mat layer below.
- Mode D_m: delaminations in the middle of the junction along both the top and the bottom edges of the wavy 90° fibre layer. A transverse crack accompanied the delaminations in the rovings either side of the mat layer.
- Mode K_m: kinking or buckling of the wavy 90° fibre layer at the middle of the junction. Kinking initiated at the point of steepest tangent angle, which for most junctions was on the AAS.

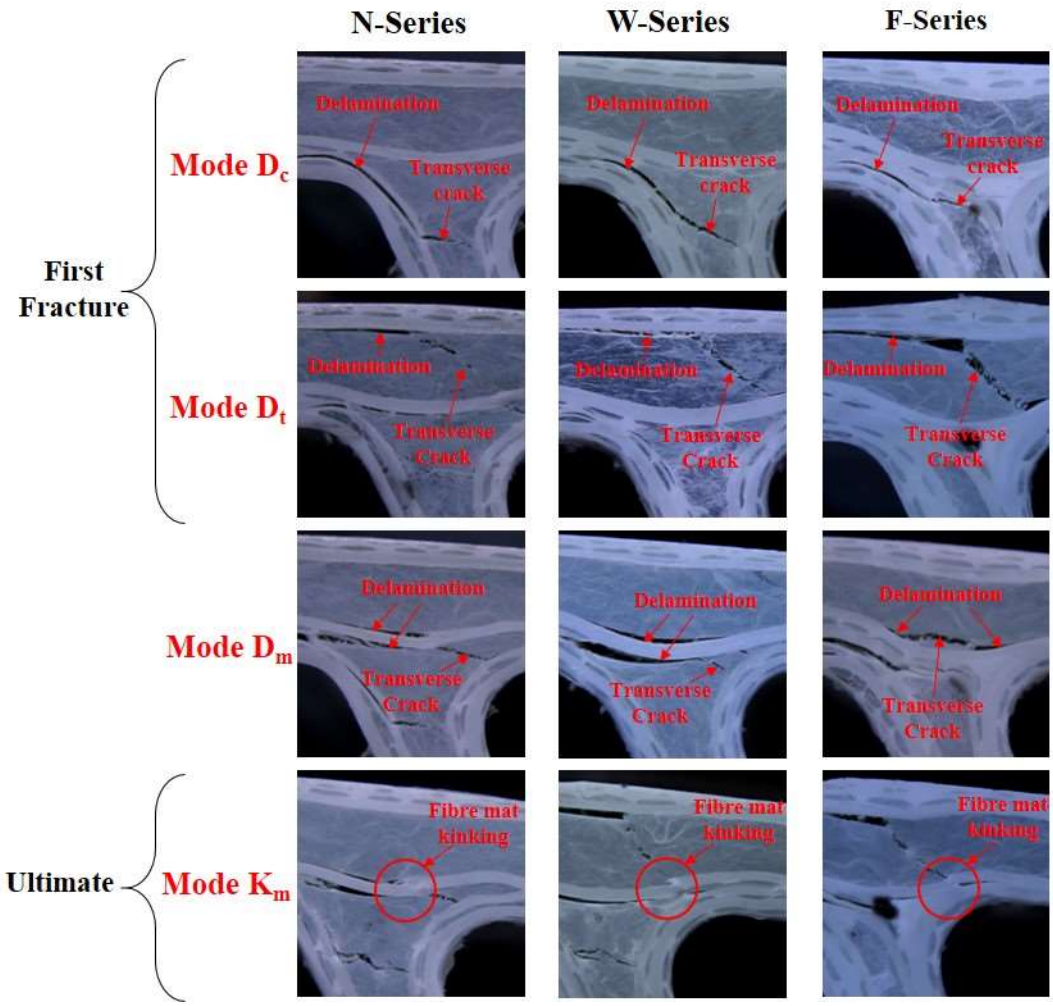

Figure 3: Classification of different damage modes observed within each junction type.

When loaded, the junctions exhibited initial linear behaviour up to a point of first fracture, which occurred in either mode D_c or D_t. When loaded further, some intermediate damage modes developed that eventually led to failure of the junction, which typically occurred in mode K_m. Figure 4 shows two examples of this damage evolution: in test W-1-70 (Figure 4(a)), first fracture initiated in mode D_t, which was followed by intermediate modes D_c and D_m, and finally the ultimate state was reached in mode K_m. In a different test (F-1-90, Figure 4(b)), only two modes developed: mode D_t at first fracture and mode K_m at ultimate. Across all tests, the sequence of damage modes was highly inconsistent and sensitive to both the lever arm of the loading and the misalignment profile within the junction.

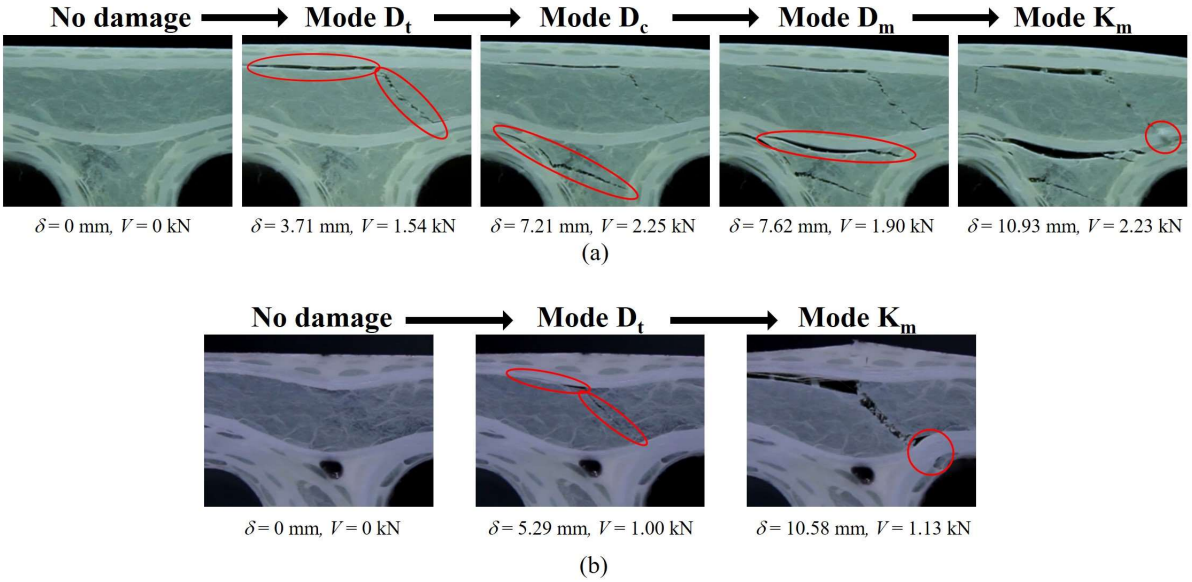

Figure 4: Examples of damage evolution in junctions under load: (a) test W-1-70 and (b) test F-1-90.

Given that, by varying the distance between the applied load and the cantilever root, the junctions were subject to various combinations of moment and shear, it is natural to define moment-shear failure envelopes for each junction type. To that end, Figure 5(a) and (b) show scatter plots of, respectively, the first fracture moment (M_f) and ultimate moment (M_u) as a function of shear (V_f, V_u). The M-V envelopes were estimated by plotting 2nd order polynomial best-fit curves, which gave the lowest R^2 values compared to other functions. For comparison, Figure 5(c) shows only the best-fit curves for both first fracture and ultimate.

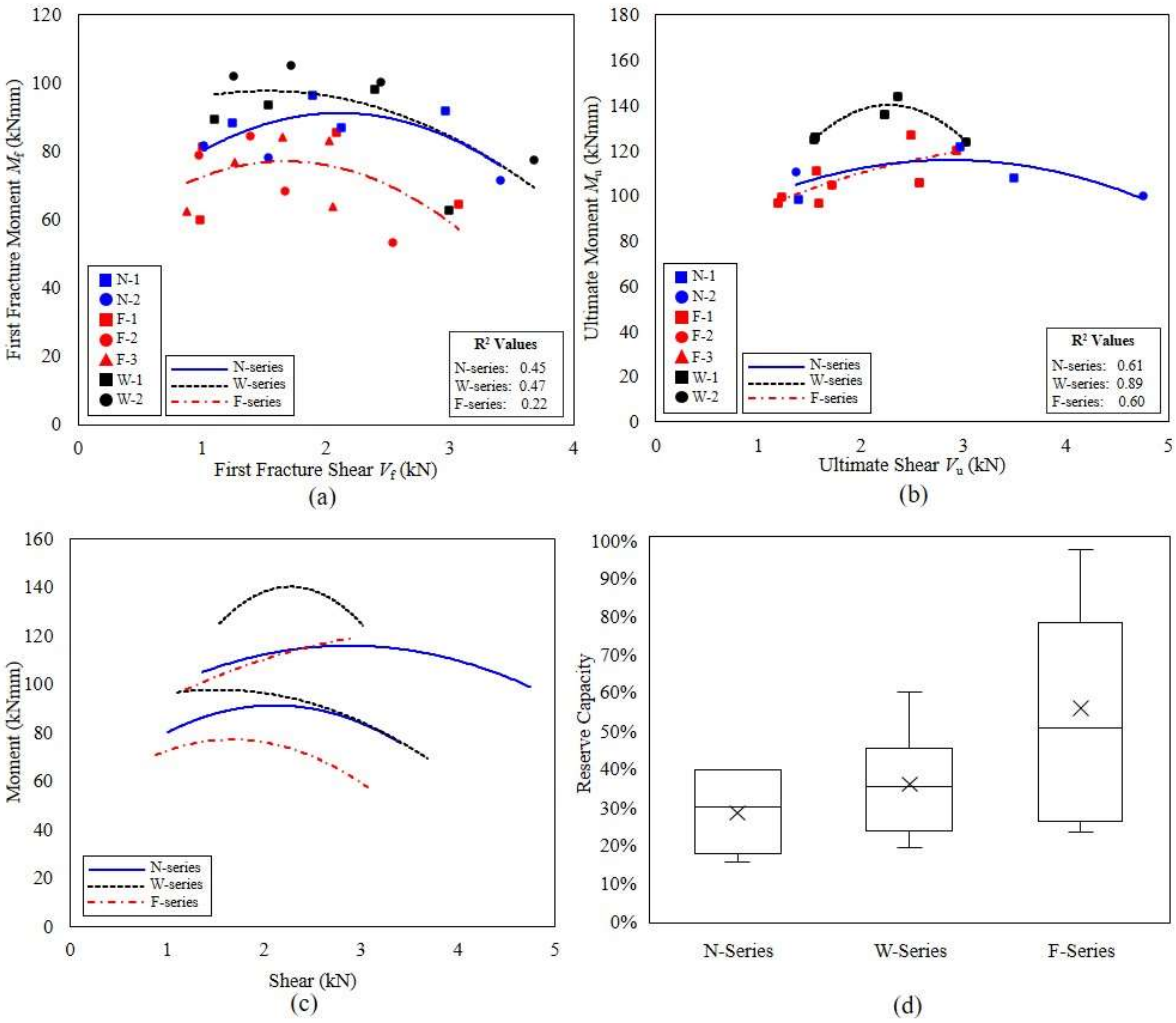

Figure 5: Moment-shear envelopes for (a) first fracture and (b) ultimate; (c) best-fit curves for both first fracture and ultimate and (d) reserve capacities for all junction types.

The *M-V* failure envelopes show several key trends:

- There is significant scatter in the moment/shear at first fracture (Figure 5(a)), although the points for each junction type are distributed primarily along the *horizontal* axis, which suggests that the first fracture was governed mostly by the applied moment. The scatter along the *vertical* axis is partially accounted for by clear differences in M_f between the junction types: compared to the W-series, M_f was on average 7% and 20% lower for the N- and F-series, respectively.
- Even within each junction type, there is still significant scatter in M_f, as evidenced by the low R^2 values shown in the bottom right corner of Figure 5(a). The N- and W- series both have R^2 values close to 0.5 and, upon closer inspection, it is seen that this scatter was primarily due to differences between the junction subgroups. For example, on average M_f was 11% lower for

W-1 (black squares) compared to W-2 (black circles), and 15% lower for N-2 (blue circles) compared to N-1 (blue squares). For the F-series, however, the points for F-1, F-2 and F-3 lie on both sides of the best-fit curve, and result in an R^2 value half that of the other junction types.

- The 'n'-shape of the envelopes in Figure 5(a) suggests that the maximum M_f was achieved only when there was a coexistent shear applied to the junction. For all junction types, the maximum moment was achieved at shear forces of between 1.5-2 kN, which equates to 19-25 kN/m width. This trend suggests that a small amount of shear *increased* the moment required to initiate first fracture up to a point, beyond which further increases in shear were detrimental.
- For ultimate (Figure 5(b)), the points are also distributed primarily along the horizontal axis, although the average M_u was approximately equal for the N- and F-series (both 19% lower than the W-series). This difference was due to the F-series having almost double the reserve capacity (the remaining load as a percentage of the first fracture load) of the N-series, as shown in Figure 5(d). Note also that the *range* of reserve capacities for the F-series was also double that of the other junction types.
- Within each junction type, the R^2 values for ultimate were all higher than for first fracture, although this was probably due to there being fewer data points, as many tests at high shear reached their ultimate state not within the junction, but rather in one of the adjoining flanges. This type of failure is explored in more detail in Section 5.1.
- The envelopes for ultimate (Figure 5(b)) are relatively flat, which suggests that the ultimate state was less sensitive to changes in shear. There was, however, a small drop-off in M_u with decreasing shear, similar to that observed for first fracture.

The inconsistency in failure behaviour is demonstrated further in Figure 6, which shows the load-displacement plots for all tests at (a) 90 mm, (b) 70 mm, (c) 50 mm and (d) 30 mm lever arm distances. These plots show the detrimental effect of damage on the load-carrying capacity of the junctions, which manifested as a sequence of load drops and concurrent reductions in tangent stiffness. Variability exists not only in the damage *loads* (exemplified by the scatter in moment-shear envelopes), but also in the damage *severity*, as indicated by the magnitude of load drops and tangent stiffness reductions up to failure. The load-displacement plots also point to further inconsistency of the initial stiffness, which one would expect to be identical for all tests at the

same lever arm distance. However, at 90 mm (Figure 6(a)) the initial stiffness was clearly greater for the N-series than for the F-series.

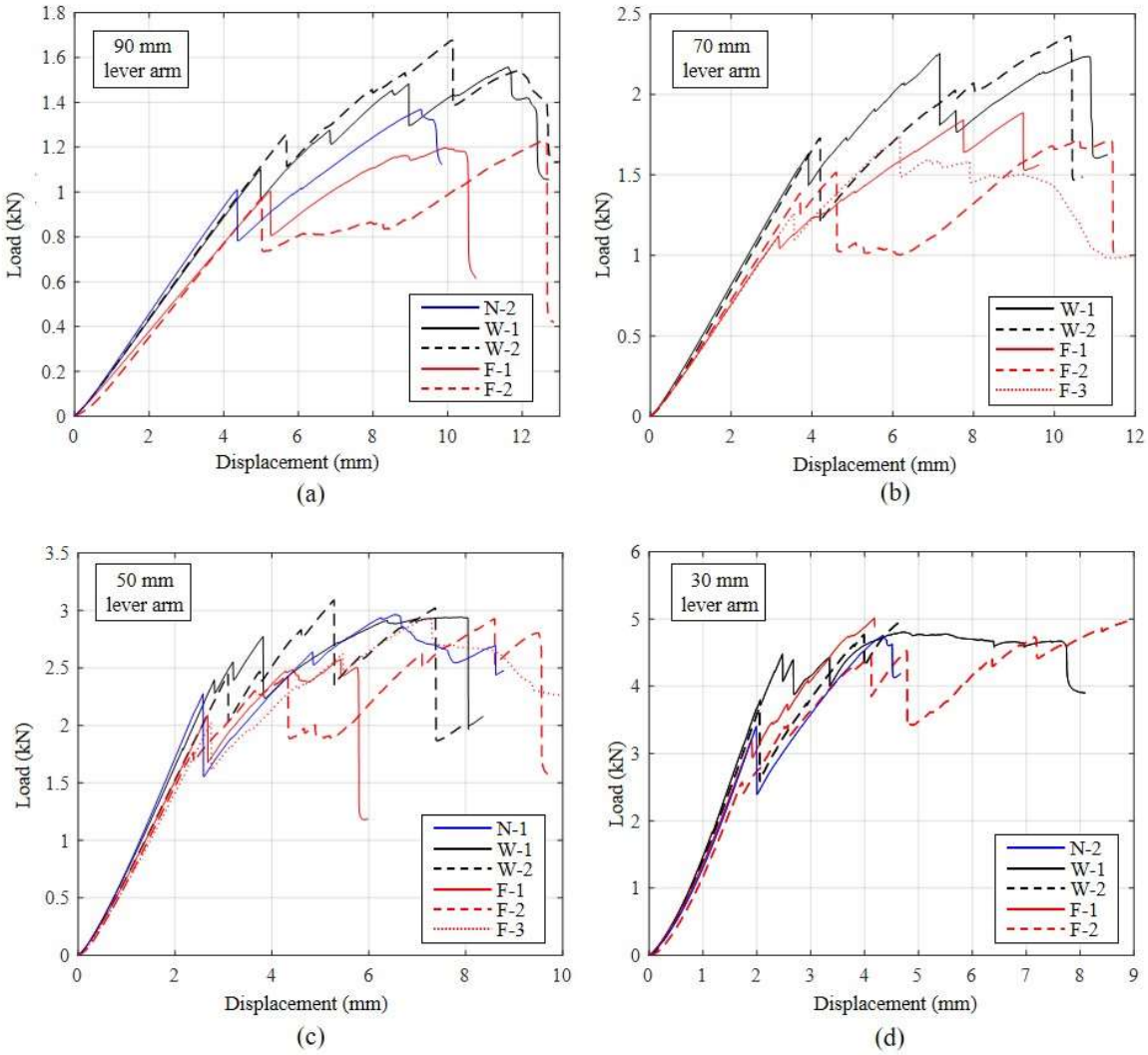

Figure 6: Load-displacement curves for all tests at (a) 90 mm, (b) 70 mm, (c) 50 mm and (d) 30 mm.

In summary, there was significant scatter in moment/shear at both first fracture and ultimate of nominally identical junctions. That some – but not all – of this scatter was accounted for by separating out the different junction types (N-, W- and F- series), suggests a strong influence of mat misalignment profile on failure. Hence, a more detailed characterisation of both the degree of misalignment and the damage severity is needed to fully understand this influence.

4. Influence of misalignment profile on ultimate behaviour

The previous section showed that damage in the junctions manifested in four distinct modes (shown in Figure 3). An important observation is that each mode can be linked to one of the three different categories of misalignment present within the junction. Damage modes D_c ,D_t and D_m/K_m were influenced by, respectively, the flip, near-surface wrinkle and waviness. This means that, for example, the effect of near-surface wrinkles on the first fracture loads can be assessed by looking *only* at first fractures that occurred in mode D_t. Likewise, looking only at measures of damage severity for mode D_t can give additional insight into the effect of near-surface wrinkles on the junctions' load-carrying capacity. To that end, the following section presents the strategy for digitally evaluating the degree of misalignment within the junctions. Following this, a set of damage indices are defined based on the load-displacement and AE energy data for each test. These indices are then used to evaluate, in turn, the damage-inducing effects of the flip, near-surface wrinkle and waviness. The discussion at the end of the section then links the results of this analysis back to the trends in the moment-shear failure envelopes described in the previous section.

4.1 Characterisation of misalignments

The strategy for quantifying the fibre mat misalignments within each junction is described in [7]. Each junction was evaluated with respect to three independent misalignment categories:

1. Flip: as shown in Figure 7(a), for the F-series junctions, the end of the triaxial mat layer was flipped from the AAS to the OAS of the junction.
2. Waviness: as shown in Figure 7(b), the biaxial mat layer passing through the middle of the junction exhibited gradual undulations due to the non-uniform distribution of rovings either side of the layer. The severity of waviness was evaluated using the length (L_w), height (H_w) and steepest tangent angle ($\theta_{max,w}$).
3. Near-surface wrinkles: as shown in Figure 7(c), the top biaxial mat layer exhibited a wrinkle near the centreline of the junction, which took the shape of a Gaussian curve. The severity of near-surface wrinkles was evaluated using the amplitude (A_w), along with the horizontal distance between the peak and the point of maximum tangent angle (c) of the Gaussian curve fit for the wrinkle.

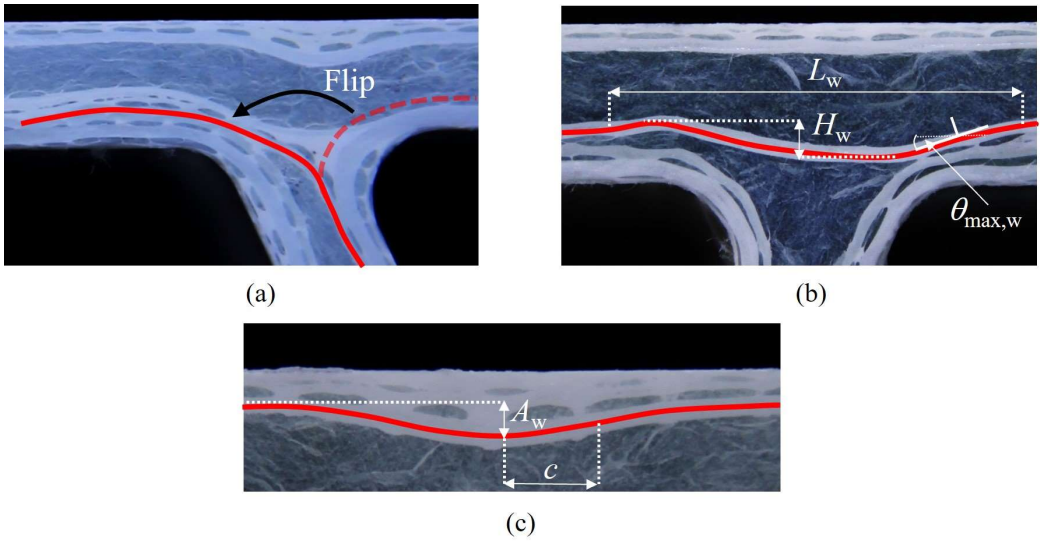

Figure 8: Characterisation of fibre mat misalignments: (a) flip, (b) waviness and (c) near-surface wrinkle.

Figure 8(a) shows a box plot of the near-surface wrinkle amplitude for each junction subgroup. On average the N-series and W-series junctions had small amplitudes of 0.28 mm and 0.34 mm, respectively, without any significant change between the specimen subgroups. Conversely, the F-series had a much greater average amplitude of 1.2 mm and there were distinct differences between the subgroups: F-2 had a 72% and 35% greater average amplitude than F-3 and F-1, respectively. This indicates that the F-1, F-2 and F-3 subgroups were produced in different pultrusion batches, all of which contained a flip, which justifies the decision made earlier to separately present data from different junction subgroups. The average wrinkle lengths for each sub-group (Figure 8(b)) did not show any significant trends between the junction types.

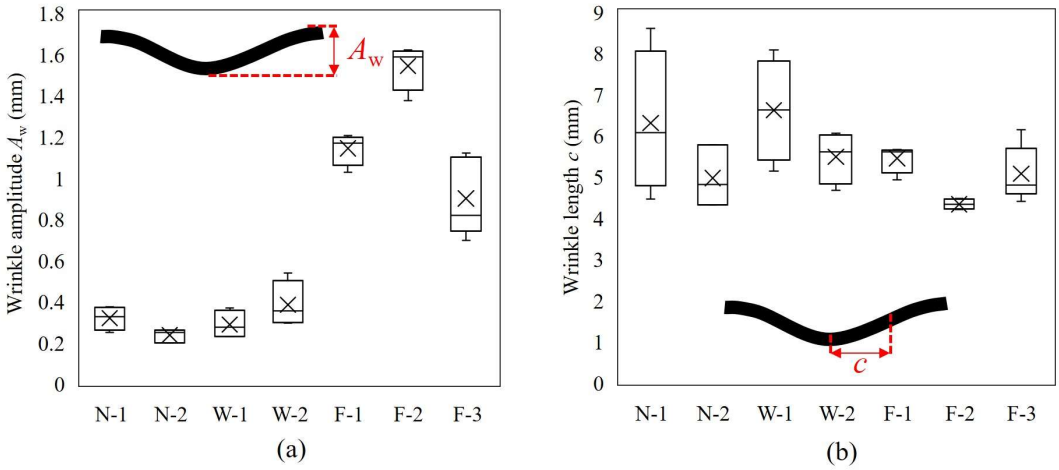

Figure 7: (a) Wrinkle amplitude and (b) wrinkle length for each specimen group.

For the horizontal biaxial mat layer passing through the junction, the average waviness height (Figure 9(a)) and steepest tangent angle (Figure 9(b)) were smallest for the N-series, with the W-series having a 36% and 32% increase in the waviness height and angle, respectively, compared to the N-series. Note that the significant waviness of the biaxial mat in the F-series specimens would have been primarily due to the flipped layer. Thus, the average waviness height and angle were 113% and 71% greater than the N-series, respectively. The waviness length (Figure 9(c)) showed no significant trends between the junction subgroups.

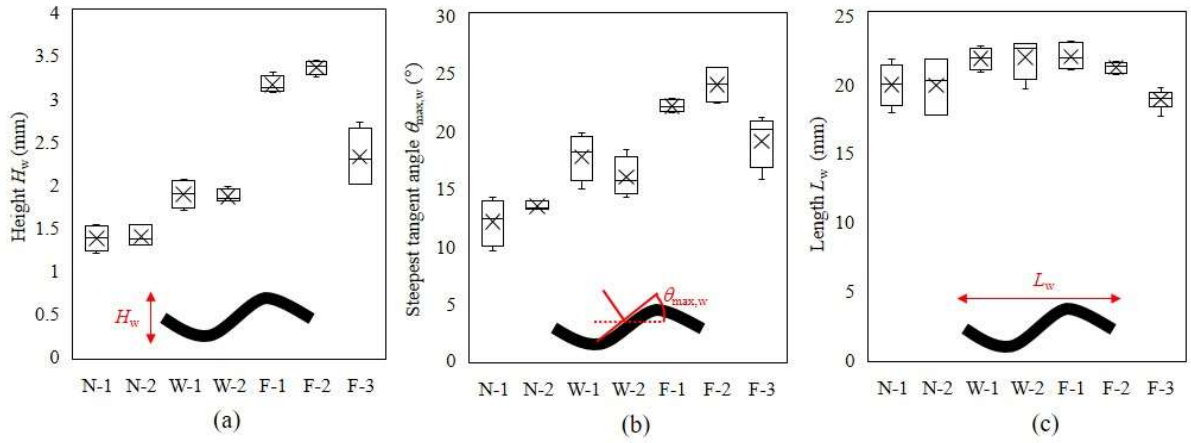

Figure 9 : (a) Waviness height, (b) steepest tangent angle and (c) length for each junction sub-group.

4.2 Definition of damage indices

The severity of damage produced within the junctions under load was characterised using three independent sources of data: load-displacement, AE energy and video. As an example, Figure 10(a) shows both load and AE energy separately plotted as a function of displacement for test W-2-50. Four damage modes developed during the W-2-50 test, which occurred in the sequence: mode D_t, mode D_c and then simultaneously modes D_c and K_m. The points at which each mode initiated are labelled in Figure 10(a), and the corresponding images are shown in Figure 10(b). The behaviour can be split into three key stages:

1. Initial linear behaviour with neither visible cracking nor significant AE emissions.
2. Sudden first fracture in mode D_t that produced a significant load drop, reduction in tangent stiffness and a single high-energy AE event (over 10^8 aJ). This was immediately followed by a dense cluster of smaller-energy AE hits, smaller load drops and a gradual reduction in tangent stiffness due to crack propagation. Then, intermediate damage developed in mode D_c that produced a load drop and high-energy AE event similar to those at first fracture.

3. Ultimate failure achieved simultaneously in modes D_m/K_m, which produced the largest load drop and AE energy event up to that point, after which the test was terminated.

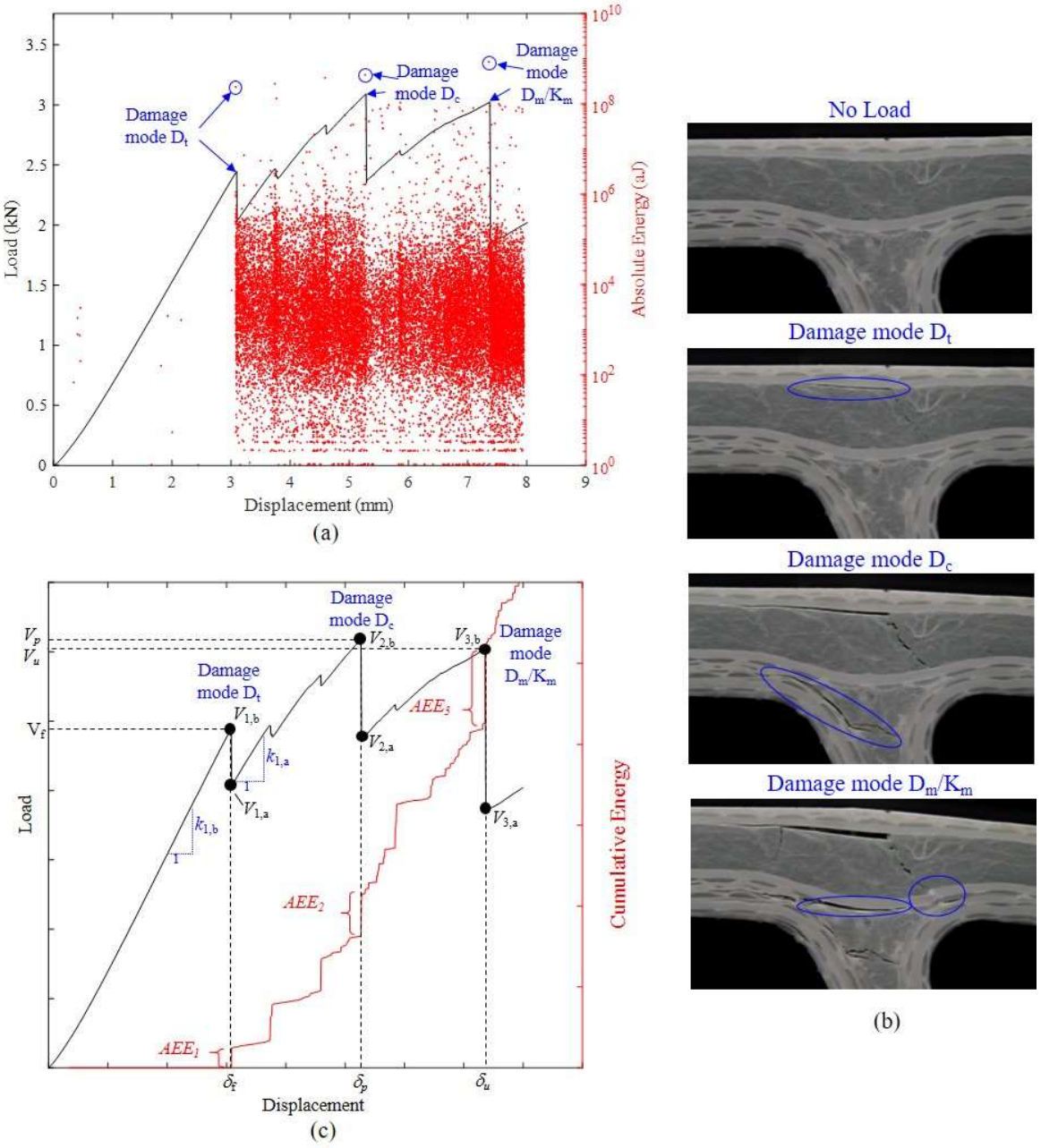

Figure 10 : Example data from test W-2-50: (a) load and AE energy vs displacement plots, (b) images of damage modes and (c) load-displacement and cumulative AE energy plots.

The load-displacement plot for this test is reproduced in Figure 10(c), but now with the AE energy more suitably presented as a *cumulative* curve. Labelled on the y-axis of this plot are the first fracture load V_f and ultimate load V_u, and on the x-axis are the corresponding displacements δ_f and δ_u. Using these plots, the first fracture is now precisely defined as the point at which AE emissions above 10^8 aJ were detected. Ultimate is

defined as the load which precipitated a load drop of at least 40%; this load drop sufficiently characterised ultimate behaviour as observed from the load-displacement plots. In the example in Figure 10(c), the peak load ($V_{p,}$ δ_p) occurred slightly *before,* and so is distinguished from, the ultimate load V_u, whereas in other tests these two loads were the same (i.e. the peak load occurred at ultimate).

From the plots in Figure 10(c), three damage indices were calculated at each damage mode initiation event n (where n = 1, 2, 3…). These were as follows:

1. Percentage load drop PLD_n, calculated as:

$$PLD_n = \frac{V_{n,b} - V_{n,a}}{V_{n,b}} \times 100 \quad (1)$$

   where $V_{n,b}$ and $V_{n,a}$ are the loads immediately before and after event n, respectively, as shown on Figure 10(c).

2. Percentage stiffness drop PSD_n, calculated as:

$$PSD_n = \frac{k_{n,b} - k_{n,a}}{k_{n,b}} \times 100 \quad (2)$$

   where $k_{n,b}$ and $k_{n,a}$ are the *tangent* stiffnesses immediately before and after event n, respectively, as shown for mode D_t in Figure 10(c).

3. Acoustic emission energy burst AEE_n (in aJ) at event n, as shown in Figure 10(c).

These indices were systematically computed for every damage initiation event for all tests. In what follows, the damage indices are used in conjunction with the moments at either first fracture M_f or ultimate M_u to analyse the influence of, alternately, the flip, near-surface wrinkle, and waviness on junction failure.

4.3 Influence of flipped layer on damage mode D_c

The flipped mat layer in the F-series junctions was adjacent to, and so would have influenced, the mode D_c damage within the OAS of the junction. Hence, Figure 11 shows box plots of (a) the first fracture moments M_f, (b) PLD_n and PSD_n values and (c) AEE_n values, all for mode D_c damage in both flipped and non-flipped junctions.

On average, the flip resulted in a 19% reduction in M_f. There was, however, still significant scatter in M_f for junctions both with and without a flip, which was likely due to variability in the bond *capacity* of the interface along which the mode A delamination occurred. The flip also resulted in a 61% increase in AE energy, but produced a 61% lower average PLD_n and a 26% lower PSD_n than junctions without a flip. This suggests that

while the flip caused damage to initiate at a lower moment, the resulting damage was less detrimental to the load-carrying capacity of the junction.

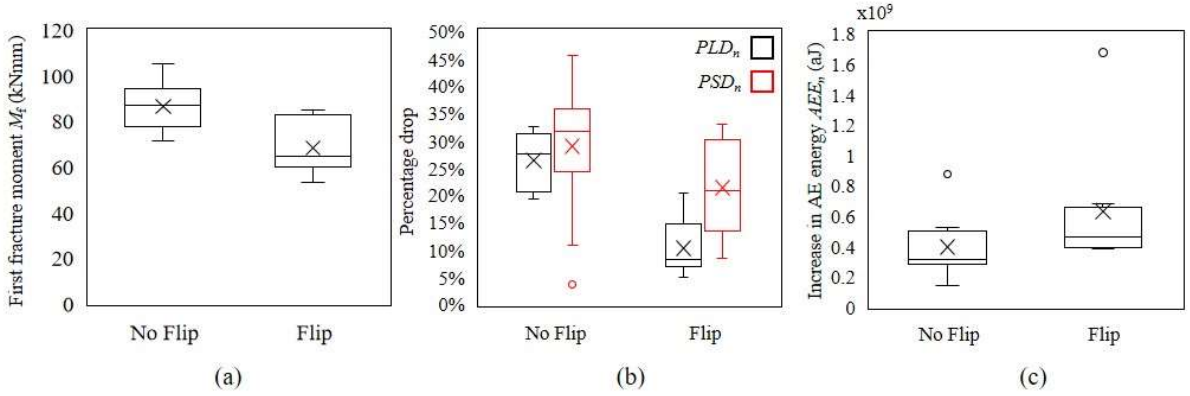

Figure 11: (a) First fracture moment M_f vs lever arm distance, (b) percentage load and stiffness drop and (c) increase in AE energy. All plots are for damage mode D_c only and compare both flipped and non-flipped junctions.

4.4 Influence of near-surface wrinkle on damage mode D_t

Damage mode D_t consisted of a delamination between the top 90° fibre and roving layers, and so would have been influenced by wrinkling this layer at the centre of the junction. This section evaluates how the wrinkle amplitude A_w influenced the initiation and severity of damage mode D_t .

First, Figure 12(a) shows the first fracture moment M_f of damage mode D_t as a function of wrinkle amplitude, with the data grouped by lever arm distance. Three additional points are plotted (in red) where mode D_t damage initiated second (all at 50 mm lever arm distance). In all cases, M_f shows a decreasing trend with increased wrinkle amplitude. Furthermore, the gradients of the linear best-fit lines are all comparable (average of -18.4 kNmm/mm). Extrapolating the linear best-fit line for the 90 mm tests backward to $A_w = 0$ shows that a wrinkle amplitude of 1.6 mm (the largest measured value) reduced M_f by 21% compared to no wrinkling.

Second, Figure 12(b), (c) and (d) show, respectively, the PLD_n, PSD_n, and AEE_n values for damage mode D_t as a function of wrinkle amplitude. The PLD_n values (Figure 12(b)) indicate that, above a threshold value of $A_w = 1$ mm, there was a strong positive correlation between PLD_n and A_w (as shown by the linear best-fit line with $R^2 = 0.82$). Similar trends are seen for both the PSD_n and the AEE_n, where the averages for $A_w > 1$ mm are, respectively, 3.0× and 3.4× higher than for $A_w < 1$ mm. Hence, mode D_t damage was consistently more severe for greater wrinkle amplitudes.

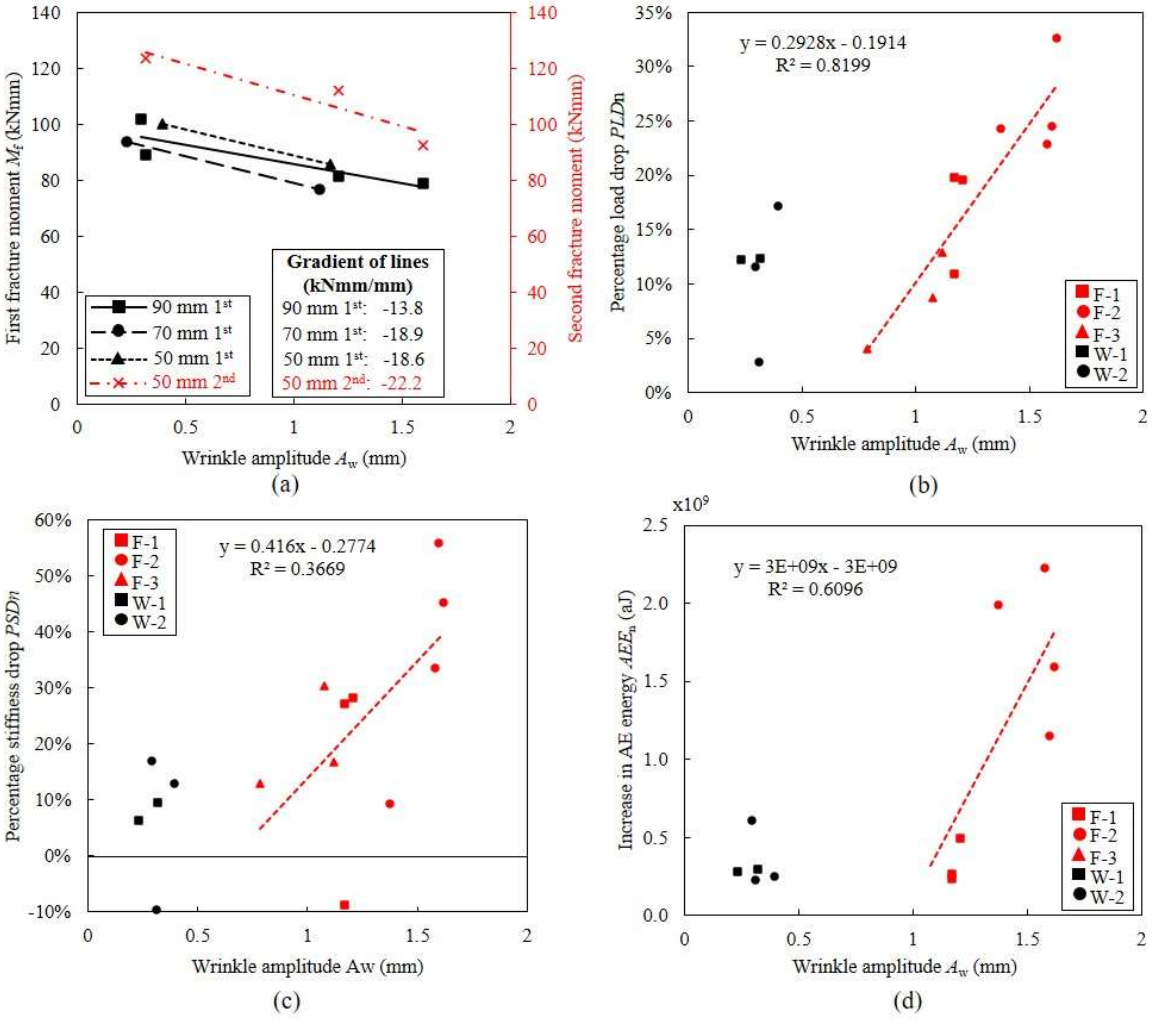

Figure 12: (a) First fracture moment M_f, (b) PLD_n, (c) PSD_n and (d) AEE_n vs wrinkle amplitude A_w. All plots are for damage mode D_t only.

An additional observation of damage mode D_t was a phenomenon called 'wrinkle-straightening'. For large wrinkle amplitudes (A_w > 1 mm), the tensile stresses in the wrinkled mat caused it to straighten out under load, as shown in Figure 13(a). Further insight into the wrinkle-straightening phenomenon is gained by examining the load-displacement and cumulative AE energy plots for tests with the largest wrinkle amplitudes.

To that end, Figure 13(b)-(e) show the load-displacement and cumulative AE curves for four tests: (a) and (b) are for junctions F-2-50 and F-2-90 (average A_w = 1.5 mm), respectively, (c) and (d) are for junctions F-1-50 and F-1-90 (average A_w = 1.1 mm), respectively. For all plots the wrinkle-straightening zone is shaded in grey. During wrinkle-straightening the load remained almost constant (i.e. the junction displayed near-zero rotational stiffness) and there was a step-change in the cumulative energy curves due to significant AE energy emissions. This burst in AE energy occurred within a finite displacement range during damage mode D_t and the increase was constant for tests at the same lever arm distance.

Figure 13 also shows that the wrinkle-straightening zone in the F-2 junctions (average A_w = 1.5 mm) occurred *immediately* after the delamination initiated by damage mode D_t, whereas in the F-1 junctions (average A_w = 1.1 mm) the wrinkle-straightening zone occurred near the end of the damage mode D_t phase. Furthermore, the total AE energy emitted during the wrinkle-straightening zone of F-2 junctions was nearly double that for F-1 junctions (1×10^{10} aJ compared to 0.5×10^{10} aJ). This suggests that an increase in wrinkle amplitude caused the wrinkle-straightening mode to occur earlier and emit more AE energy. This is especially problematic given that, as shown in Figure 13(a), wrinkle-straightening causes multiple cracks to propagate to the surface of the GFRP deck, which can act as paths for water ingress and further long-term degradation of the junction.

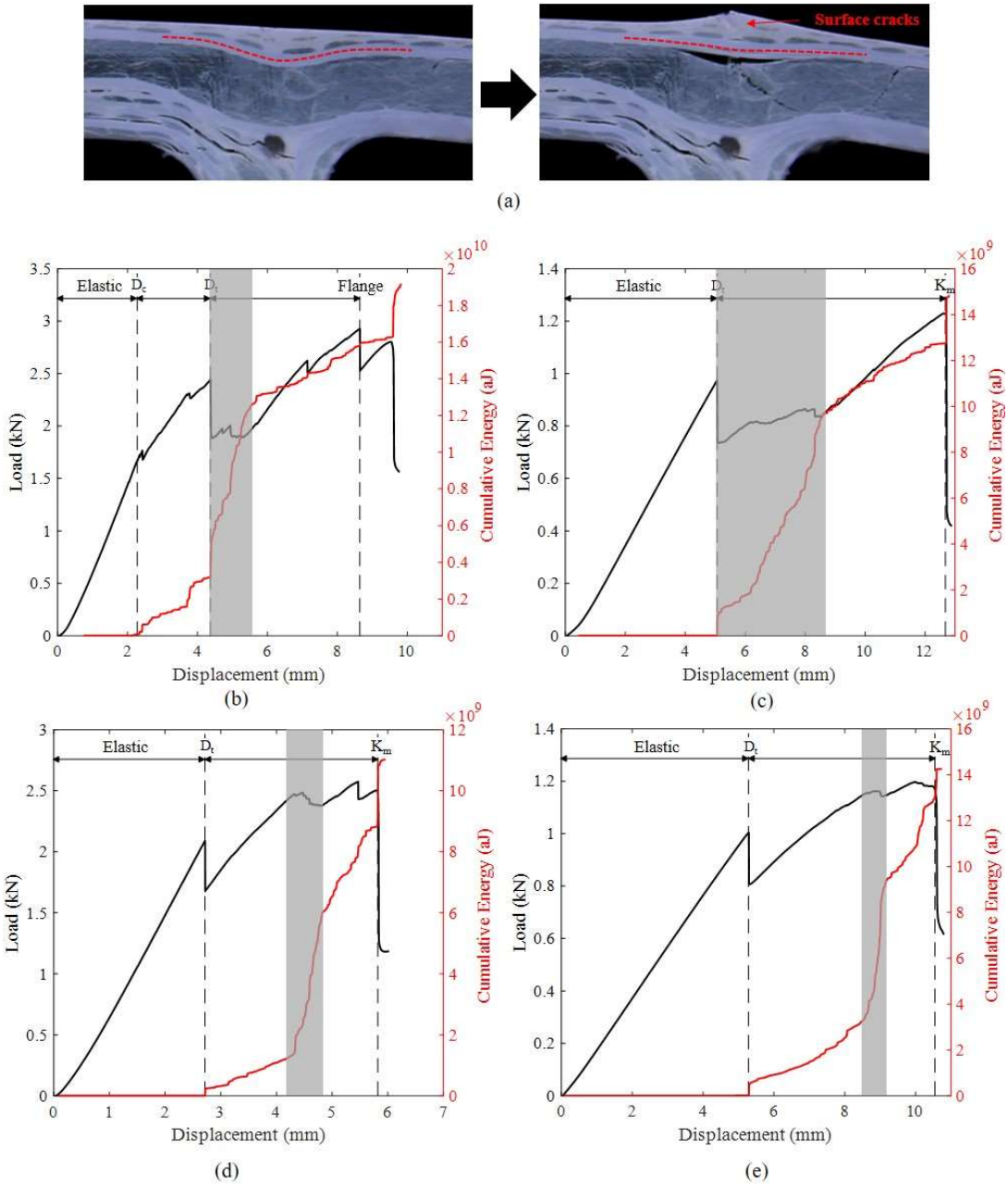

Figure 13: (a) Wrinkle-straightening during damage mode D_t for test F-2-30. Load-displacement and cumulative AE energy plots for (a) F-2-50 and (b) F-2-90 (A_w = 1.5mm), and for (c) F-1-50 and (d) F-1-90 (A_w = 1.1 mm). Wrinkle-straightening zone is shaded in grey.

4.5 Influence of waviness on damage modes D_m and K_m

The waviness of the biaxial mat layer that passed horizontally through the middle of the junction can be linked to two damage modes: mode D_m (delaminations above and below the layer) and mode K_m (kinking of the mat layer at ultimate). The analysis showed that none of the waviness parameters shown in Figure 9 (height, length or angle) had a significant correlation with the four indices for damage mode D_m. This is likely due to all mode D_m events having a PLD_n of less than 5%, which means that most mode D_m events did not significantly influence the load-carrying capacity of the junction.

There was, however, a negative correlation between the maximum waviness angle $\theta_{max,w}$ and the ultimate moment M_u within damage mode K_m. This relation is shown in Figure 14(a), where the moments are grouped by lever arm distance and a linear best-fit line has been fitted through all points. Extrapolating the linear best-fit line back to $\theta_{max,w} = 0°$ shows that a waviness angle of 26° (the largest measured value) reduced M_u by 35% compared to no waviness. This value should be viewed with caution, however, given the significant

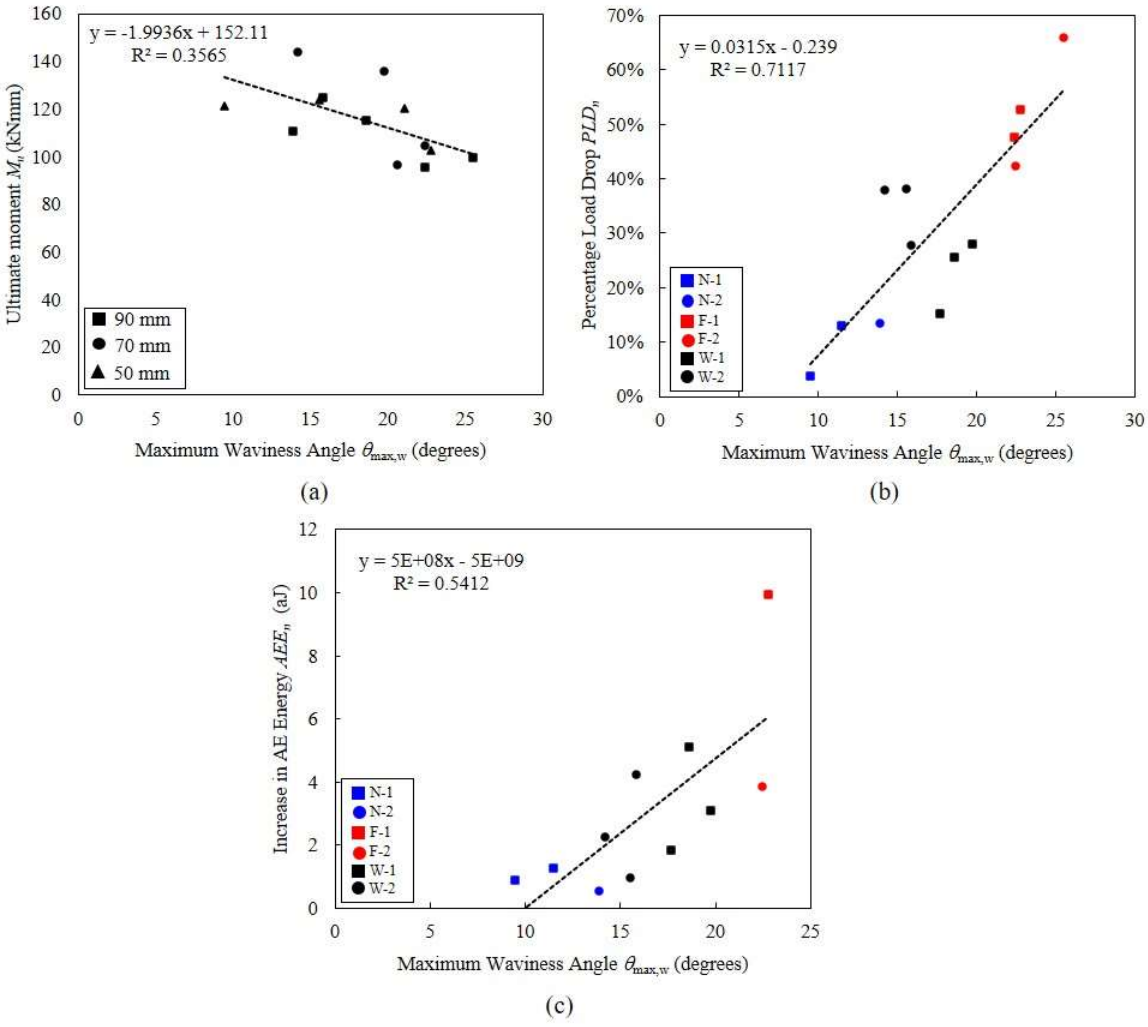

Figure 14: (a) PLD_n vs maximum waviness angle $\theta_{max,w}$ and (b) AEE_n vs maximum waviness angle $\theta_{max,w}$ for damage mode K_m.

scatter ($R^2 = 0.36$) that is due primarily to the influence of the junctions' damage history on the ultimate moment.

The PLD_n and AEE_n values for damage mode K_m are shown in Figure 14(b) and (c), respectively. There was a strong positive correlation in both cases; the R^2 values from a linear best-fit line were higher for the PLD_n data (0.712) than for the AEE_n data (0.541). It is important to note that the R^2 values for M_u, PLD_n and AEE_n were all higher than equivalent values using either the waviness height H_w or length L_w. This indicates that the waviness *angle* accounts for more of the variance in the junctions' failure. This is to be expected, given that the kinking always initiated at the point of steepest tangent angle. In both Figure 14(b) and (c), the indices significantly increase after a threshold angle of approximately 10°.

4.6 Linking results to moment-shear envelopes

Using the results from the systematic analysis of each misalignment and the associated damage presented above, some of the key trends in the moment-shear failure envelopes in Figure 5 can now be explained.

First, the low first fracture moments (M_f) of the F-series were a consequence of both the flip (which reduced M_f for damage mode D_c by 19%) and the near-surface wrinkle (which reduced M_f for damage mode D_t by up to 21%). The wide range of wrinkle amplitudes (from 0.8 mm to 1.6 mm) in the F-series was likely responsible for the increased scatter in M_f compared to other junction types. Although, for junctions both with and without a flip, there was still significant scatter within damage mode D_c that cannot be a consequence of the increased stress *demand* due to mat misalignment. Instead, this is likely due to variable stress *capacities* at the interface between the fibre layers along which delamination occurred.

Second, the W-series had a slightly higher (7%) average M_f than the N-series, despite having a similar near-surface wrinkle amplitude. One explanation for this is that, as can be seen in the images in Figure 3, for the W-series the mode D_c delamination occurred between the complex mat and roving layers, whereas for the N-series the delamination occurred between the +45° and -45° layers within the triaxial mat. Hence, the bond strength of the complex mat/roving interface may have been greater than the +45°/-45° interface, leading to an increase in M_f in the W-series.

Further evidence of the high bond strength at the complex mat/roving interface of the W-series is seen in Figure 15, which shows horizontal bar charts indicating the displacement at which a specific damage mode initiated during the test. It is seen that first fracture occurred in mode D_c for only 25% of W-series junctions,

compared to 100% of N-series junctions. This again indicates that the W-series had a relatively high bond strength at the location of mode D_c damage, which, coupled with the small near-surface wrinkle amplitude, likely explains the higher M_f for the W-series junctions.

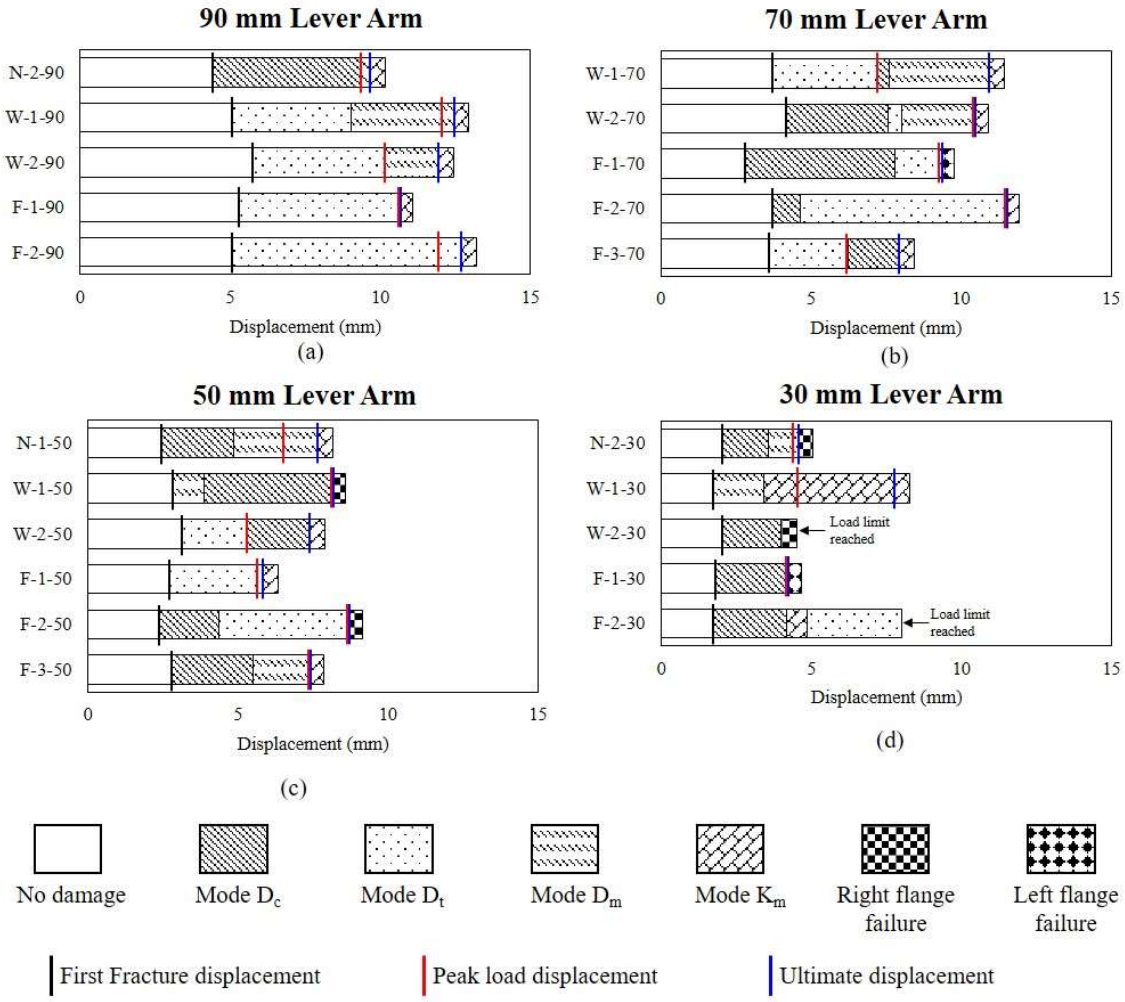

Figure 15: Evolution of damage modes for junctions tested at (a) 90 mm, (b) 70 mm, (c) 50 mm and (d) 30 mm.

Third, Figure 15 also provides insight into why the M_f initially increased and then rapidly decreased as a function of shear, resulting in the 'n'-shaped envelopes seen in Figure 5(a). Although the damage evolution was highly inconsistent across all tests, at a 90 mm lever arm 80% of first fractures occurred in mode D_t, while at a 30 mm lever arm 80% of first fractures occurred in mode D_c. This suggests a transition from mode D_t at low shear to mode D_c at high shear, although there was no consistent point at which the mode switch occurred. Thus, it is reasonable to conclude that, for damage mode D_t, a small increase in shear force may have *reduced* the stress demand at the interface between the top fibre mat and roving layers, and hence *increased* the moment required to initiate delamination. Further increases in shear, however, switched the dominant damage mode to a delamination within the OAS of the junction (mode D_c), which led to a subsequent reduction in M_f.

The above hypothesis appears to be contradicted by the N-series envelope, which also shows a drop-off in M_f at low shear despite the first fracture always occurring in mode D_c. However, by looking at the points in Figure 5(a) for N-1 (blue squares) and N-2 (blue circles) separately, it is seen that they both lie approximately on a horizontal line with a slight negative gradient, which is consistent with the above hypothesis. The overall 'n'-shape of the N-series envelope is due to the average M_f of N-2 being 15% lower than N-1, combined with the N-2 junctions being tested at a wider range of lever arms than N-1.

Finally, Figure 15 also indicates that for many tests ultimate failure did not occur within the junction, but rather within the adjoining flanges. This is why the ultimate moment-shear envelopes in Figure 5(b) have far fewer points than for first fracture. This mode of failure is discussed in the following section.

5. Other consequences of misalignment

5.1 Flange damage

In 26% of tests, the ultimate state did not occur within the junction, but instead was caused by a fracture within the AAS flange (19% of tests) or the OAS flange (7% of tests). Examples of both flange fractures are shown in Figure 16(a) and (b). It is seen that these fractures were the result of near-surface wrinkles in the top biaxial mat, which led to a delamination between this mat and the rovings, as well as a transverse crack through the rovings. Some specimens had flange wrinkles of amplitudes up to 2 mm, which significantly compromised the deck's load-carrying capacity and therefore such specimens should not be used in a real structure.

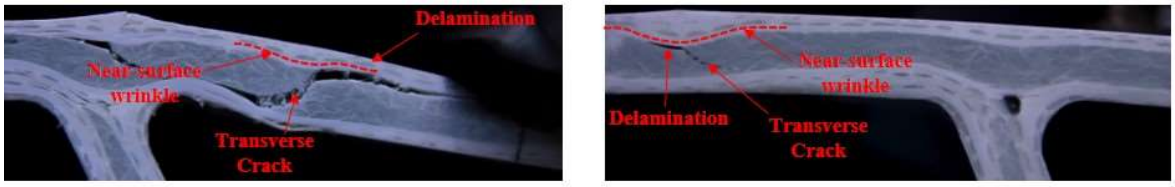

a) b)

Figure 16: Examples of (a) failure within the right-hand flange of test F-2-50 and (b) failure within left-hand flange of test F-1-70. Note in both cases the right-hand flange was the cantilever.

To compare the severity of flange damage to that of the other four modes within the junction, Figure 17 shows box plots of (a) the percentage load drop PLD_n, (b) the percentage stiffness drop PSD_n and (c) the

increase in AE energy AEE_n for damage modes D_c, D_t, D_m and K_m, as well as for the flange damage on the junction's AAS (denoted 'flange').

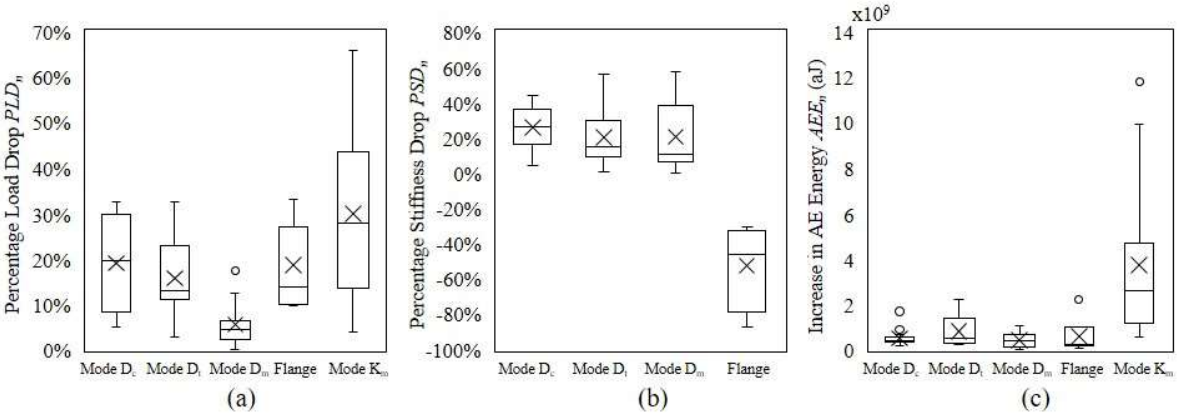

Figure 17: Comparison of (a) percentage load drop, (b) percentage stiffness drop and (c) AE energy burst for each failure mode within the junctions and also for flange failure.

Figure 17(a) shows that the average PLD_n for flange damage was comparable to modes D_c and D_t. Figure 17(b) shows, however, that flange damage always produced a substantial *increase* in tangent stiffness (52% on average). As an example of this effect, Figure 18 shows the load-displacement data for test F-2-50, and Figure 18(b) provides a magnified view of the region at which flange damage occurred. It is seen that, prior to flange damage, the tangent stiffness gradually decreased from (1) to (2), at which point flange damage precipitated a 14% drop in load to (3). The new tangent stiffness immediately after (3) was comparable to that at (1), where the points (1) and (3) are at the same load. This suggests that flange damage caused a redistribution of stresses that changed the load-resisting mechanism of the cantilever in a way that increased the tangent stiffness.

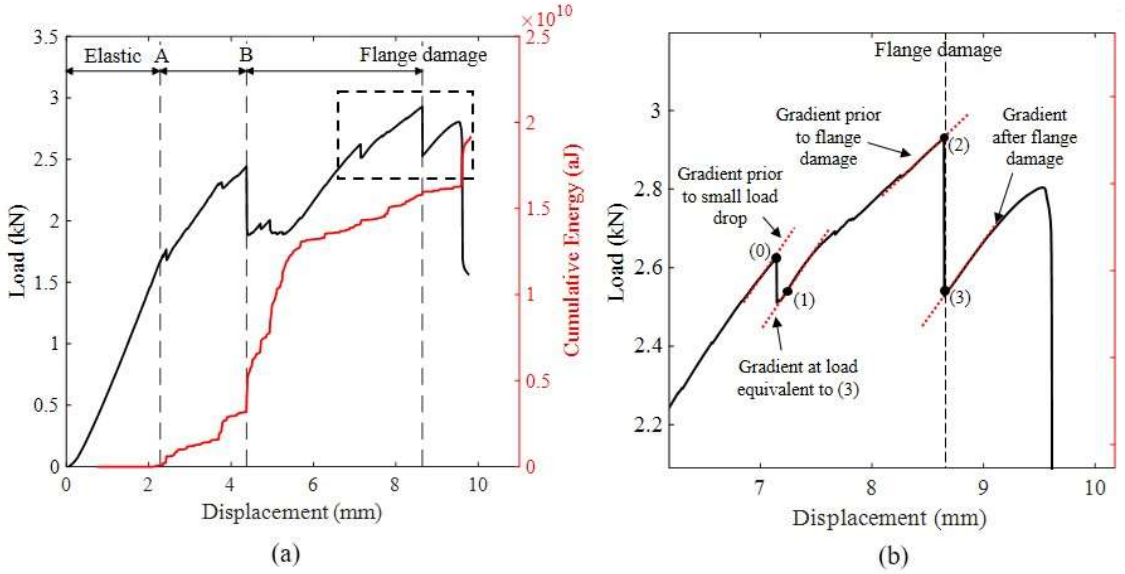

Figure 18: (a) Load-displacement and cumulative AE plots for test F-2-50, (b) magnified plot at location of flange damage.

In addition to some damage events causing an increase in stiffness, Figure 18(b) also shows that a small – but still significant – load drop at (0) caused no reduction in tangent stiffness. Indeed, the data for PSD_n shown previously in Figure 17(b) indicates that many damage events caused no reduction in tangent stiffness. This suggests that the change in tangent stiffness is not a reliable measure of damage.

5.2 Variation of initial stiffness

Figure 19 plots the initial stiffness of all junctions before the first fracture event ($k_{1,b}$) as a function of lever arm distance. The initial stiffness was calculated from the gradient of the load-displacement curve from approximately 50% of the first fracture load up to just before the first load drop. This was to avoid the small 'bedding-in' effect observed for some specimens. Figure 19 shows some scatter in the initial stiffnesses from tests conducted at the same lever arm distance, which increases from 90 mm to 30 mm. This is to be expected, given the smaller displacements at shorter lever arm distances, which increases the percentage error in the measurements.

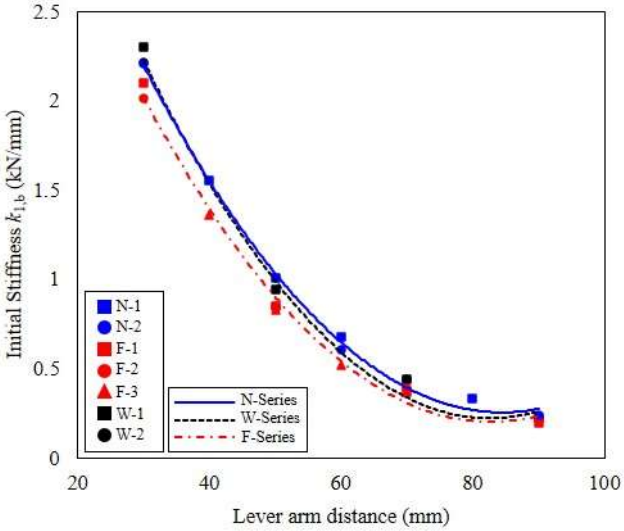

Figure 19 : Initial stiffness vs lever arm distance for all tests.

At 90 mm, where there is minimal scatter, the initial stiffnesses of the W-series and F-series junctions were 7.1% and 17.8% lower than the N-series junctions, respectively. These changes in stiffness are mostly explained by the variation in cantilever thicknesses t_c, which were 8.60 mm, 8.31 mm and 8.02 mm for the N-, W- and F- series, respectively. Recall that these changes in thickness were a result of differential displacement of the internal mandrels during pultrusion, which, in turn, were caused by asymmetrical pressures acting on the mandrel due to the fibre mat misalignments [7]. For example, for the junctions containing a flip (F-series), the average flange thickness on the AAS was 8.02 mm and on the OAS was 9.15 mm. This difference is directly attributable to the triaxial mat layer being flipped from the AAS to the OAS of the junction.

A simplified beam-theory model of the cantilever, which assumes that the junctions provide fully-fixed support conditions and that the GFRP material is homogeneous, predicts that the gradient of the load-displacement curve is proportional to the second moment of area of the cantilever, which, in turn, is proportional to the cube of the flange thickness. This model predicts a 9.8% and 18.9% reduction in the initial stiffnesses of the W- and F- series compared to the N-series, respectively. These reductions are comparable to the measured reductions at a 90 mm lever arm distance (7.1% and 17.8%, respectively). It should be noted, however, that the assumptions made in this calculation are overly simplistic. For example, the transverse fibres are not uniformly distributed, but rather sandwiched either side of the longitudinal fibres. Hence, flanges of different thicknesses will have the same volume of transverse fibres, but the distance between the top and bottom layers will vary. Furthermore, misalignments including those shown in Figure 16 will produce variable mechanical properties along the length of the cantilever.

6. Conclusions

Nominally identical junctions of a pultruded GFRP bridge deck containing different fibre mat misalignment profiles were loaded to ultimate. Repeat tests were performed while moving the load location along the adjoining flange to apply different combinations of moment and shear to the junction. The following conclusions can be drawn from this study:

- When loaded, the junctions developed four distinct damage modes, each of which was linked to a specific category of fibre mat misalignment. The initiation of each damage mode produced a pronounced load drop and corresponding high-energy AE event. Both the sequence of damage and the associated loads were sensitive to the lever arm of loading and to the misalignment profile.
- The moment-shear envelopes showed significant scatter for both first fracture and ultimate. The shape of the envelopes suggested a gradual increase and then a rapid decrease in first fracture moment as a function of shear. This trend was linked to a switch in damage mode from a delamination between the top fibre mat and roving layers at low shear, to a delamination within the obtuse angle side of the junction at high shear.
- Junctions with a flipped mat initiated damage at a 19% lower moment and with 61% more AE energy than junctions with no flip, but the resulting load and tangent stiffness drops were 61% and 26% lower, respectively.

- Wrinkling of the fibre mat at the top of the junction reduced the first fracture moment by up to 21% compared to no wrinkling. For wrinkle amplitudes greater than 1 mm, the average percentage load drop, percentage stiffness drop and AE energy emitted were, respectively, 2.0×, 3.0× and 3.4× higher than for amplitudes less than 1 mm. Also, amplitudes greater than 1 mm produced 'wrinkle-straightening', during which the junction exhibited near-zero rotational stiffness and emitted significant AE energy.
- Waviness of the fibre mat in the middle of the junction reduced the ultimate moment by up to 35% compared to no waviness.
- In 27% of tests, damage occurred within the flange, which often resulted in an *increase* in tangent stiffness. This suggests that by itself the change in tangent stiffness is not a reliable measure of damage.
- The variable thicknesses of the top flange on the acute angle side of the junction, which was another consequence of the misalignments, caused reductions in initial stiffness of up to 18%.

These findings can be used to inform quality standards for pultruded profiles to include limitations on the existence of certain types of misalignments, including the flip shown in Figure 7(a), or on the severity of misalignment. For example, the damage caused by near-surface wrinkles at the centre of the junction rapidly increased for amplitudes greater than 1 mm (approximately, 10% of the part thickness), likewise for maximum waviness angles of greater than 10°. These could be used as limiting values for the severity of misalignment within pultruded sections.

This paper has shown how the scatter in failure loads of nominally identical junctions can be accounted for in part by the increase in stress *demand* resulting from misalignment of the fibre mats. Further work is needed, however, to evaluate the variability of stress *capacities* that also contributes to scatter in failure loads, for which digital image correlation may be a valuable tool. Such data can help validate multi-layered FE analyses of the progressive failure of the junctions, which would enable the trajectory of individual mat layers to be altered to predict the optimum load-carrying capacity of the junctions when subjected to local tyre loading.

7. References

[1] Keller T. Overview of fibre-reinforced polymers in bridge construction. Struct Eng Int J Int Assoc Bridg Struct Eng 2002;12:66–70.

[2] Mosallam AS, Bayraktar A, Elmikawi M, Pul S, Adanur S. Polymer Composites in Construction: An Overview. SOJ Mater Sci Eng 2014;2:01–25.

[3] Hollaway LC. A review of the present and future utilisation of FRP composites in the civil infrastructure with reference to their important in-service properties. Constr Build Mater 2010;24:2419–45.

[4] Poulton M, Sebastian W. Tyre load fatigue of cellular FRP bridge decks. Adv. Compos. Constr. ACIC 2019 - Proc. 9th Bienn. Conf. Adv. Compos. Constr. 2019, 2019, p. 33–8.

[5] Luke S, Canning L, Collins S, Knudsen E, Brown P, Taljsten B, et al. Advanced composite bridge decking system - Project ASSET. Struct Eng Int J Int Assoc Bridg Struct Eng 2002;12:76–9.

[6] Sebastian WM, Johnson M. Interpretation of sensor data from in situ tests on a transversely bonded fibre-reinforced polymer road bridge. Struct Heal Monit 2019;18:1074–91.

[7] Poulton M, Sebastian W. Taxonomy of fibre mat misalignments in pultruded GFRP bridge decks. Compos Part A Appl Sci Manuf 2021;142:106239.

[8] Keller T, Gürtler H. Quasi-static and fatigue performance of a cellular FRP bridge deck adhesively bonded to steel girders. Compos Struct 2005;70:484–96.

[9] Sebastian WM, Keller T, Ross J. Influences of polymer concrete surfacing and localised load distribution on behaviour up to failure of an orthotropic FRP bridge deck. Compos Part B Eng 2013;45:1234–50.

[10] Gabler M, Knippers J. Improving fail-safety of road bridges built with non-ductile fibre composites. Constr Build Mater 2013;49:1054–63.

[11] Yanes-Armas S, de Castro J, Keller T. Energy dissipation and recovery in web-flange junctions of pultruded GFRP decks. Compos Struct 2016;148:168–80.

[12] Xin H, Mosallam A, Liu Y, Wang C, Zhang Y. Impact of hygrothermal aging on rotational behavior of web-flange junctions of structural pultruded composite members for bridge applications. Compos Part B Eng 2017;110:279–97.

[13] Xin H, Mosallam A, Liu Y, Yang F, Zhang Y. Hygrothermal aging effects on shear behavior of pultruded FRP composite web-flange junctions in bridge application. Compos Part B Eng 2017;110:213–28.

[14] Xin H, Mosallam A, Liu Y, Wang C. Hygrothermal aging effects on axial behaviour of pultruded web–flange junctions and adhesively bonded build-up bridge members. J Reinf Plast Compos 2018;37:13–34.

[15] Xin H, Mosallam A, Liu Y, Wang C, Zhang Y. Analytical and experimental evaluation of flexural behavior of FRP pultruded composite profiles for bridge deck structural design. Constr Build Mater 2017;150:123–49.

[16] Wang Y, Zureick AH. Characterization of the longitudinal tensile behavior of pultruded I-shape structural members using coupon specimens. Compos Struct 1994;29:463–72.

[17] Bank LC, Yin J, Nadipelli M. Local buckling of pultruded beams - nonlinearity, anisotropy and inhomogeneity. Constr Build Mater 1995;9:325–31.

[18] Turvey GJ, Zhang Y. Shear failure strength of web-flange junctions in pultruded GRP WF profiles. Constr Build Mater 2006;20:81–9.

[19] Turvey GJ, Zhang Y. Characterisation of the rotational stiffness and strength of web-flange junctions of pultruded GRP WF-sections via web bending tests. Compos Part A Appl Sci Manuf 2006;37:152–64.

[20] Turvey GJ, Zhang Y. Tearing failure of web-flange junctions in pultruded GRP profiles. Compos Part A Appl Sci Manuf 2005;36:309–17.

[21] Liu TQ, Yang JQ, Feng P, Harries KA. Determining rotational stiffness of flange-web junction of pultruded GFRP I-sections. Compos Struct 2020;236:111843.

[22] Sebastian W, Dodds B, Benner C. Commentary: Restoring the west mill GFRP deck road bridge to full capacity. Proc Inst Civ Eng Struct Build 2020;173:158–60.

[23] Sebastian WM. Bi-axial behaviours of abraded and rehabilitated FRP decks as anisotropic plates under concentrated wheel loading. Eng Struct 2021;233:111704.

[24] Potter K, Khan B, Wisnom M, Bell T, Stevens J. Variability, fibre waviness and misalignment in the determination of the properties of composite materials and structures. Compos Part A Appl Sci Manuf 2008;39:1343–54.

[25] Hassan MH, Othman AR, Kamaruddin S. A review on the manufacturing defects of complex-shaped laminate in aircraft composite structures. Int J Adv Manuf Technol 2017;91:4081–94.

[26] Thor M, Sause MGR, Hinterhölzl RM. Mechanisms of Origin and Classification of Out-of-Plane Fiber Waviness in Composite Materials—A Review. J Compos Sci 2020;4:130.

[27] Nelson JW, Riddle TW, Cairns DS. Effects of defects in composite wind turbine blades-Part 1: Characterization and mechanical testing. Wind Energy Sci 2017;2:641–52.

[28] Weber TA, Englhard M, Arent JC, Hausmann J. An experimental characterization of wrinkling generated during prepreg autoclave manufacturing using caul plates. J Compos Mater 2019;53:3757–73.

[29] Sebastian WM. Fibre waviness in pultruded bridge deck profiles: Geometric characterisation and consequences on ultimate behaviour. Compos Part B Eng 2018;146:270–80.

[30] Sápi Z, Butler R, Rhead A. Filler materials in composite out-of-plane joints – A review. Compos Struct 2019;207:787–800.

[31] Trask RS, Hallett SR, Helenon FMM, Wisnom MR. Influence of process induced defects on the failure of composite T-joint specimens. Compos Part A Appl Sci Manuf 2012;43:748–57.

[32] Bloom LD, Wang J, Potter KD. Damage progression and defect sensitivity: An experimental study of representative wrinkles in tension. Compos Part B Eng 2013;45:449–58.

[33] Altmann A, Gesell P, Drechsler K. Strength prediction of ply waviness in composite materials considering matrix dominated effects. Compos Struct 2015;127:51–9.

[34] Mukhopadhyay S, Jones MI, Hallett SR. Tensile failure of laminates containing an embedded wrinkle; numerical and experimental study. Compos Part A Appl Sci Manuf 2015;77:219–28.

[35] El-Hajjar RF, Petersen DR. Gaussian function characterization of unnotched tension behavior in a carbon/epoxy composite containing localized fiber waviness. Compos Struct 2011;93:2400–8.

[36] Godin N, Reynaud P, Fantozzi G. Acoustic emission and durability of composite materials. ISTE Ltd, John Wiley & Sons, Inc; 2018.

[37] Saeedifar M, Zarouchas D. Damage characterization of laminated composites using acoustic emission: A review. Compos Part B Eng 2020;195:108039.

[38] Brunner AJ, Terrasi GP. Acousto-ultrasonic signal analysis for damage detection in GFRP adhesive joints. J Acoust Emiss 2008;26:152–9.

[39] Brunner AJ, Terrasi GP, Vallee T, Keller T. Acoustic Emission Analysis and Acousto-Ultrasonics for Damage Detection in GFRP Adhesive Joints. 28th Eur Conf AE Test 2008:100–5.

[40] Fiberline. The bridge that dissapeared 2019. https://fiberline.com/cases-construction/bridges/the-bridge-

that-disappeared/ (accessed January 6, 2021).

[41] British Standards Institution. BS ISO 15114:2014 Fibre-reinforced plastic composites - Determination of the mode II fracture resistance for unidirectionally reinforced materials using the calibrated end-loaded split (C-ELS) test and an effective crack length approach. Br Stand 2014:18.

[42] ASTM International. ASTM E976-15 “Standard Guide for Determining the Reproducibility of Acoustic Emission Sensor Response.” West Conshohocken, Pennsylvania, USA: 2015.